Supporting Information: Electrode potential governs oxygen–oxygen bond formation through coupled interfacial dynamics

Ritika Saroha and Swastika Banerjee*

Department of Chemistry, Indian Institute of Technology Roorkee, 247667, Uttarakhand, India

E-mail: sbanerjee@cy.iitr.ac.in

Computational Methods

Electronic structure calculations

Density functional theory (DFT) calculations were performed using the Vienna *Ab initio* Simulation Package (VASP),[1] employing the projector-augmented-wave (PAW) method to describe electron–ion interactions.[2] To establish a reliable description of the structural and interlayer interactions in Nb_2Se_2C, the PBE, RPBE, SCAN and PBEsol exchange–correlation functionals were assessed alongside D2, D3 and many-body dispersion (MBD) corrections.

Structural optimizations employed a plane-wave kinetic-energy cutoff of 520 eV and a Γ-centred Monkhorst–Pack sampling scheme with a reciprocal-space spacing of $0.04(2\pi\ \text{Å}^{-1})$. The electronic energy and atomic-force convergence thresholds were set to 10^{-5} eV and 10^{-2} eV Å^{-1}, respectively.

Grand-canonical constant-potential implementation

The electrified Nb_2Se_2C/water interface was simulated using the constant-potential hybrid-solvation dynamics model (CP-HS-DM) implemented in CP-VASP.[3,4] The immediate electrode–electrolyte interface was described using explicit water molecules, while the surrounding solution was represented by the polarizable continuum model implemented in VASPsol.[5]

Constant-potential conditions were maintained by coupling the electronic system to a fictitious potentiostat,[6] which dynamically adjusts the electron population in response to deviations between the instantaneous and target electrode potentials. At successive control intervals, the electron population was updated according to

$$n_i = n_{i-1} + C(U_d - U), \tag{1}$$

where n_i and n_{i-1} denote the electronic populations at successive control intervals, C is the effective interfacial capacitance, and U_d and U are the prescribed and instantaneous electrode potentials, respectively.

The instantaneous electrode potential was referenced to the standard hydrogen electrode (SHE) through

$$-eU = E_F - e\phi - \left(E_F^{\mathrm{SHE}} - e\phi^{\mathrm{SHE}}\right), \tag{2}$$

where E_F is the Fermi energy and ϕ is the electrostatic potential evaluated in the bulk-like implicit-solvent region. The reference term $\left(E_F^{\mathrm{SHE}} - e\phi^{\mathrm{SHE}}\right)$ was taken as 4.6 eV, following the VASPsol calibration.[5]

During constant-potential molecular dynamics, the electron population was updated every five integration steps, allowing the electrode charge to respond dynamically to interfacial structural changes. Charge compensation by the implicit electrolyte maintained overall electrostatic neutrality within the simulation model. In contrast, the constant-charge simulations were performed at a fixed electronic population.

Molecular dynamics simulation parameters

Ab initio molecular dynamics (AIMD) simulations were performed in the canonical (NVT) ensemble at 300 K using a Nosé –Hoover thermostat and a time step of 1 fs. A plane-wave kinetic-energy cutoff of 400 eV and Γ-point sampling were employed to reduce the computational cost of dynamical simulations.

The interfacial water structure was initially equilibrated under constant-charge conditions, followed by equilibration with the hybrid-solvation environment. Constant-potential simulations were subsequently performed with grand-canonical electron updates to examine the potential-dependent evolution of adsorbed oxygen species and the surrounding electrolyte.

Constrained dynamics and Blue-Moon ensemble sampling

The direct O–O coupling pathway was investigated using constrained AIMD within the slow-growth framework.[7] The composite reaction coordinate, defined in the main text, couples the formation of the O–O bond with the evolution of the two surface Nb–O bonds.

The reaction coordinate was advanced at a constant rate of -2×10^{-3} Å fs^{-1}, enabling continuous sampling of the transformation from adjacent surface-bound oxo species towards the O–O-coupled product.

For equilibrium constrained sampling, the mean force along the reaction coordinate can be evaluated using the Blue-Moon ensemble formalism:[8]

$$\frac{dW}{d\varepsilon} = \frac{\left\langle Z^{-1/2}\left(-\lambda + k_{\mathrm{B}}TG\right)\right\rangle_{\varepsilon}}{\left\langle Z^{-1/2}\right\rangle_{\varepsilon}}, \tag{3}$$

where λ denotes the Lagrange multiplier associated with the geometric constraint, k_{B} is the Boltzmann constant and T is the simulation temperature. The mass-metric factor Z is defined as

$$Z = \sum_i \frac{1}{m_i} \left(\frac{\partial \varepsilon}{\partial r_i} \right)^2, \tag{4}$$

and the corresponding geometric correction is

$$G = Z^{1/2} \sum_{ij} \frac{1}{m_i m_j} \frac{\partial \varepsilon}{\partial r_i} \frac{\partial^2 \varepsilon}{\partial r_i \partial r_j} \frac{\partial \varepsilon}{\partial r_j}. \tag{5}$$

Here, m_i and r_i represent the atomic masses and Cartesian coordinates, respectively.

The geometric constraint was imposed using the SHAKE algorithm,[9] which introduces a Lagrange multiplier into the system Lagrangian:

$$L^*(r, p, \varepsilon) = L(r, p) + \lambda \left[\varepsilon(r) - \varepsilon \right]. \tag{6}$$

For a continuously evolving reaction coordinate, the accumulated work can be expressed as

$$W_{\text{pull}} = \int_{t_1}^{t_2} \frac{\partial H}{\partial \varepsilon} \dot{\varepsilon} \, dt. \tag{7}$$

In the quasistatic limit, the accumulated work approaches the reversible free-energy difference. At finite pulling rates, however, dissipative contributions may arise, and the work profile does not necessarily coincide with the equilibrium potential of mean force. The connection between nonequilibrium work and equilibrium free-energy differences can be established through appropriate work-distribution approaches.[10]

Nonadiabatic coupling implementation

Nonadiabatic coupling (NAC) calculations were performed using CA-NAC,[11] which evaluates electronic-state couplings using the concentric approximation within the PAW formalism.

The time-dependent coupling matrix elements were calculated from wavefunction overlaps between consecutive molecular dynamics configurations using the symmetric finite-difference

formulation of Hammes-Schiffer and Tully.[12]

For nondegenerate electronic states, the coupling can also be related to the nuclear derivative of the electronic Hamiltonian:

$$D_{jk}(t) = \frac{\left\langle \phi_j \left| \nabla_{\mathbf{R}} \hat{H} \right| \phi_k \right\rangle \cdot \dot{\mathbf{R}}}{\epsilon_k - \epsilon_j}, \tag{8}$$

where ϵ_j and ϵ_k are the corresponding Kohn–Sham eigenvalues, $\hat{H}$ is the electronic Hamiltonian and $\dot{\mathbf{R}}$ denotes the nuclear velocity. The concentric approximation was used to evaluate the wavefunction overlaps required for the finite-difference NAC calculation. Matrix elements were evaluated independently at each sampled **k**-point and subsequently averaged over the Brillouin-zone sampling mesh. Electronic states within an energy window of $E_F \pm 0.5$ eV were included to characterize the near-Fermi electronic response associated with O–O coupling and Nb–O bond rearrangement. The resulting NAC distributions were analysed along the constrained reaction coordinate under constant-charge and constant-potential conditions. These calculations characterize the strength and evolution of electron–nuclear coupling accompanying the reaction but do not, independently, determine nonadiabatic transition probabilities.

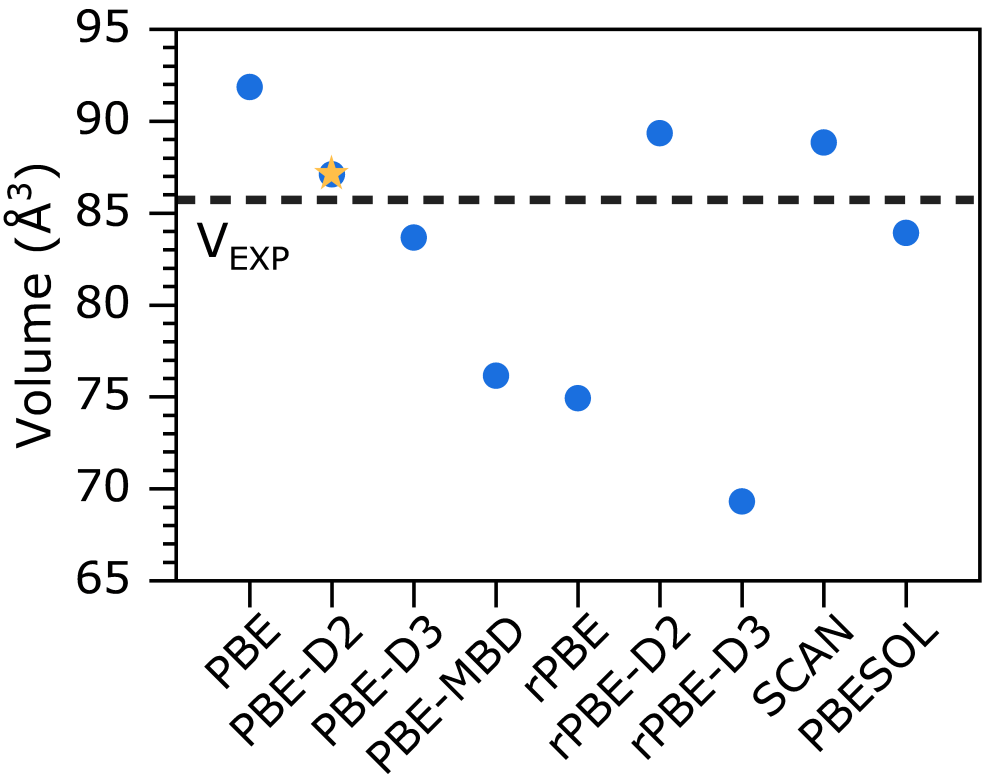

Figure S1: **Validation of the computational method against experiment.** Calculated unit-cell volume ($\AA^3$) of the system obtained with different exchange-correlation functionals and dispersion corrections (PBE, PBE-D2, PBE-D3, PBE-MBD, rPBE, rPBE-D2, rPBE-D3, SCAN and PBEsol). The dashed horizontal line marks the experimental volume (V_{EXP} =85.61$\AA^3$) . The functional used in this work, PBE-D2, is highlighted with star.

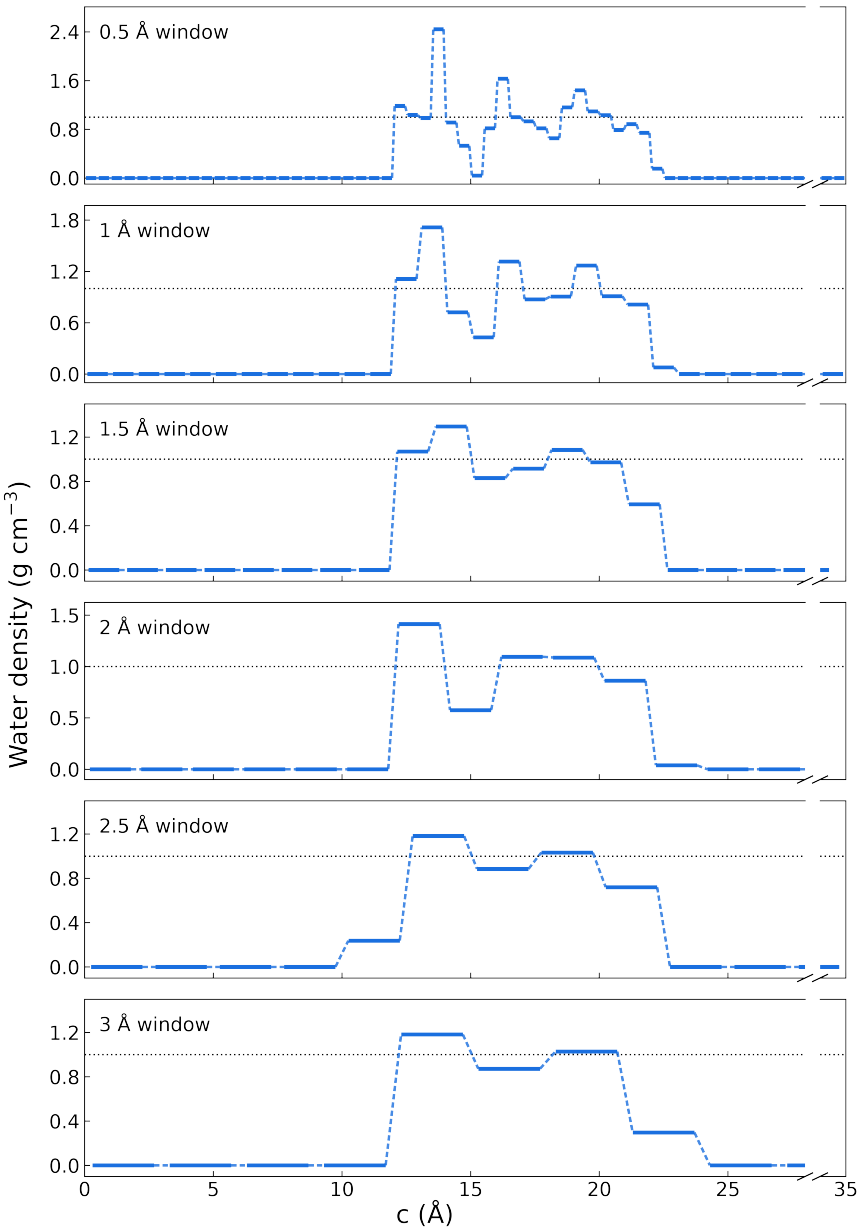

Figure S2: **Sensitivity of the interfacial water-density profile to the spatial averaging window.** Time-averaged water-density profiles along the surface-normal (c) direction at the $(1\bar{1}0)$ Nb_2Se_2C/H_2O interface, evaluated using spatial averaging windows from 0.5 to 3.0 Å in increments of 0.5 Å. The horizontal dashed line denotes the bulk-water density (1.0 g cm^{-3}) as a reference.

The principal density features and their positions remain largely preserved across the investigated range, whereas increasing the window progressively smooths local density fluctuations. A window of 0.5 Å was therefore adopted for the main-text analysis.

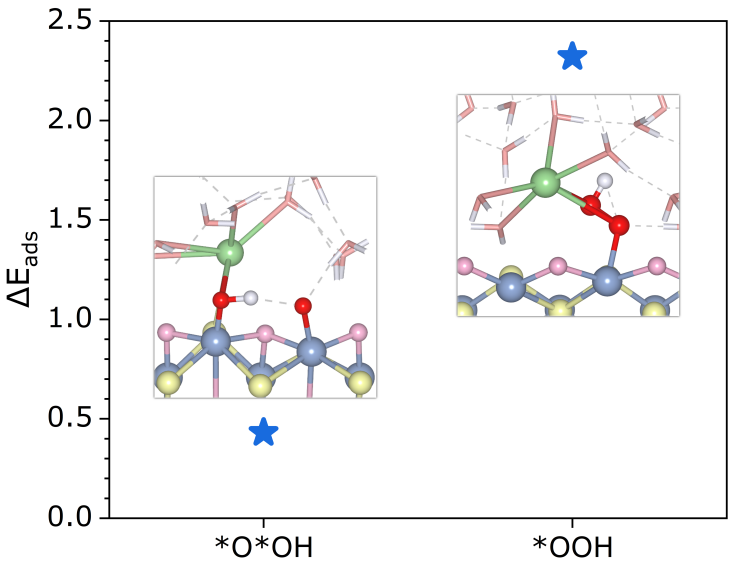

Figure S3: **Comparison of the AEM and OPM intermediates at the Nb_2Se_2C/water interface in the presence of solvated K:**Adsorption energies (ΔE_{ads}, in eV) of the *O*OH intermediate, characteristic of the oxide path mechanism (OPM), and the *OOH intermediate, characteristic of the conventional adsorbate evolution mechanism (AEM). The insets show representative AIMD snapshots of the corresponding interfacial configurations.

On Nb_2Se_2C/water interface, *O*OH is stabilized with $\Delta E_{ads} \approx 0.4$eV, whereas *OOH is considerably less favorable with $\Delta E_{ads} \approx 2.3$eV, indicating that the cation-assisted OPM is thermodynamically preferred over the AEM.

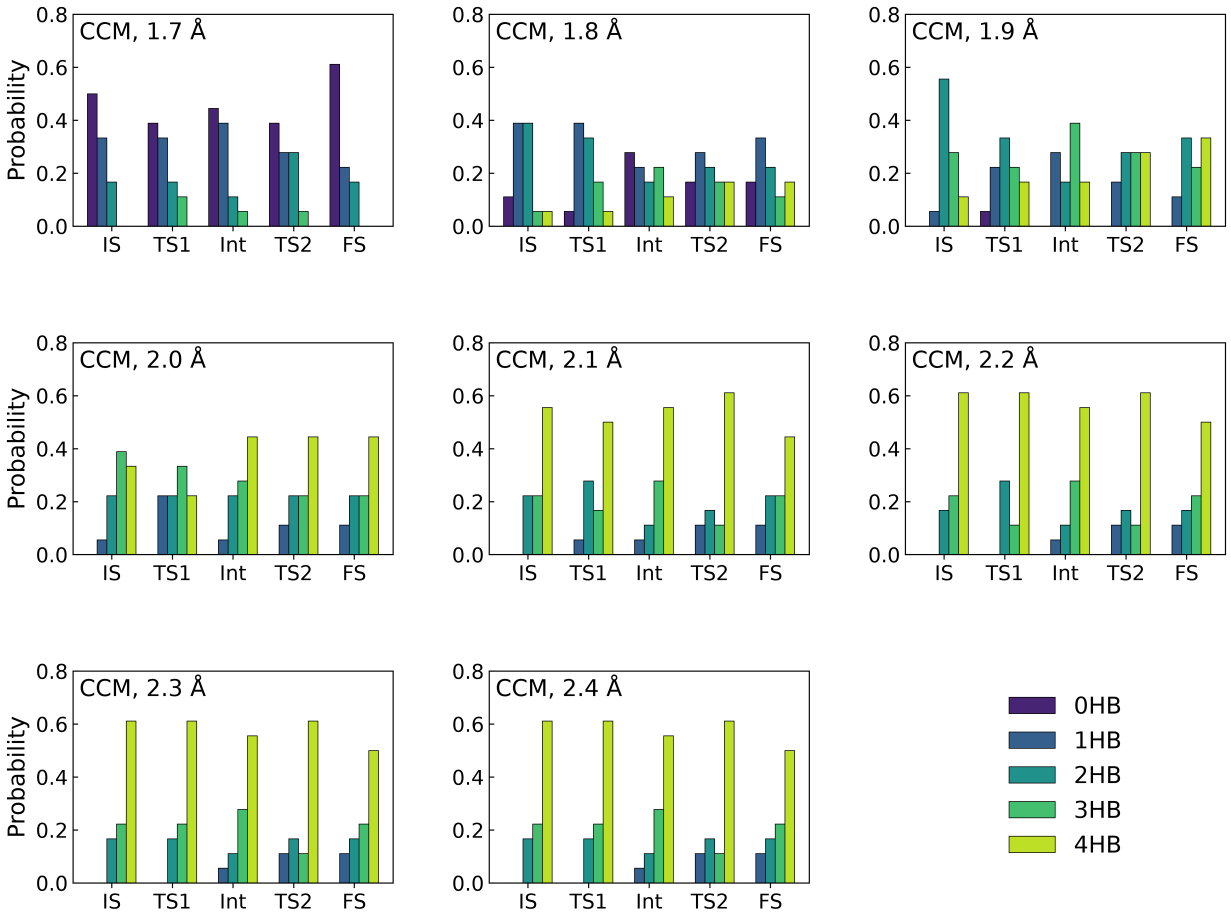

Figure S4: **Sensitivity of the hydrogen-bond statistics to the H—O distance cutoff under CCM:** Probability distributions of water molecules forming n hydrogen bonds with neighboring water molecules (n HB, $n = 0$–4) at each state along the collective variable (IS, TS1, Int, TS2, and FS), evaluated for H–O distance cutoffs varied from 1.7Å to 2.4Å in increments of 0.1Å

At the shortest cutoff (1.7Å), the distributions are dominated by the 0HB and 1HB populations, whereas at cutoffs of 2.1Å and above, the 4HB population prevails in all states and the distributions become nearly invariant with respect to the cutoff, indicating saturation at the highly coordinated end and loss of discriminating power among the hydrogen-bonding environments. The intermediate cutoff of 1.8Å resolves the full range of hydrogen-bonding environments (0HB–4HB) without saturating at either extremum and was therefore adopted in the main text (Fig. 5b: left)

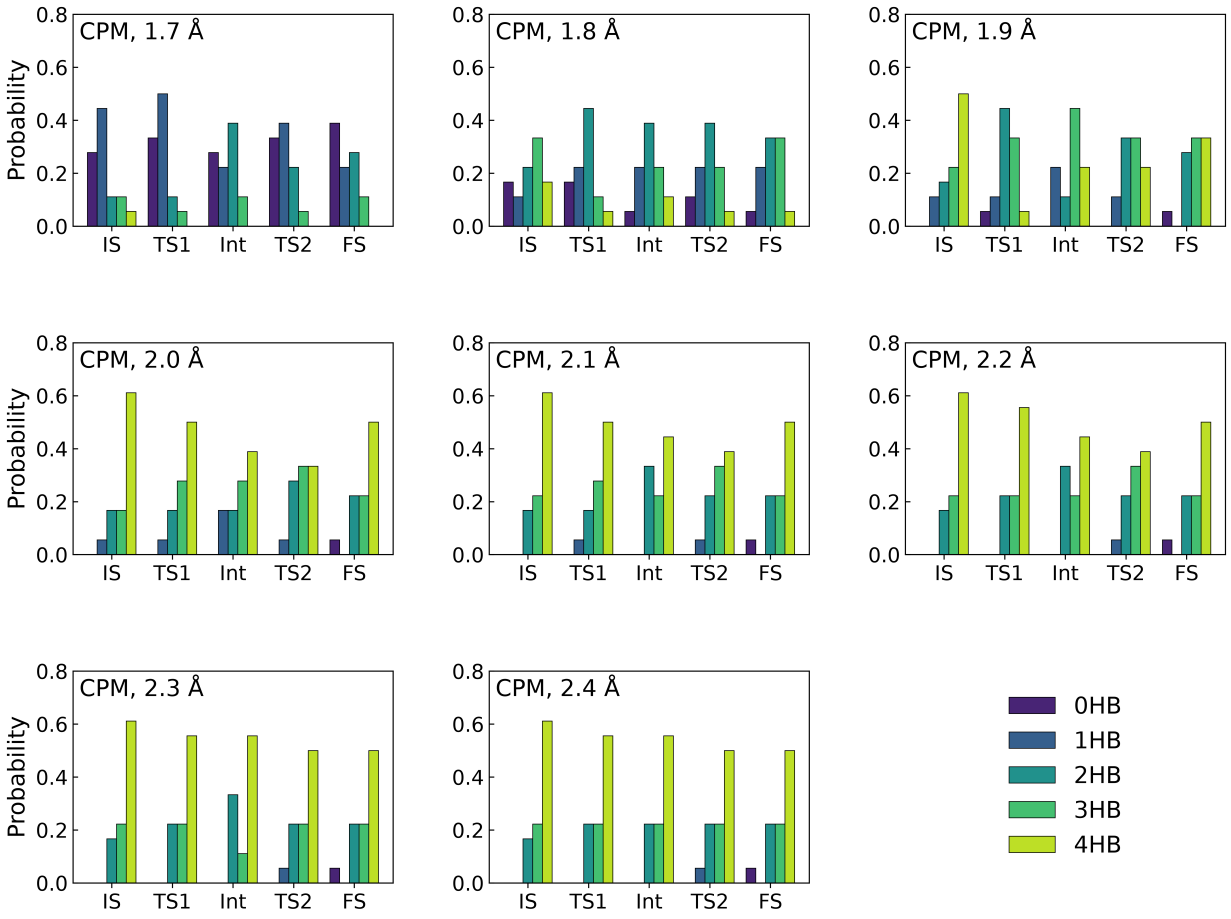

Figure S5: **Sensitivity of the hydrogen-bond statistics to the H—O distance cutoff under CPM:** Probability distributions of water molecules forming n hydrogen bonds with neighboring water molecules (n HB, $n = 0$–4) at each state along the collective variable (IS, TS1, Int, TS2, and FS), evaluated for H–O distance cutoffs varied from 1.7Å to 2.4Å in increments of 0.1Å

At the shortest cutoff (1.7Å), the distributions are dominated by the 0HB and 1HB populations, whereas at cutoffs of 2.1Å and above, the 4HB population prevails in all states and the distributions become nearly invariant with respect to the cutoff, indicating saturation at the highly coordinated end and loss of discriminating power among the hydrogen-bonding environments. The intermediate cutoff of 1.8Å resolves the full range of hydrogen-bonding environments (0HB–4HB) without saturating at either extremum and was therefore adopted in the main text (Fig. 5b: right)

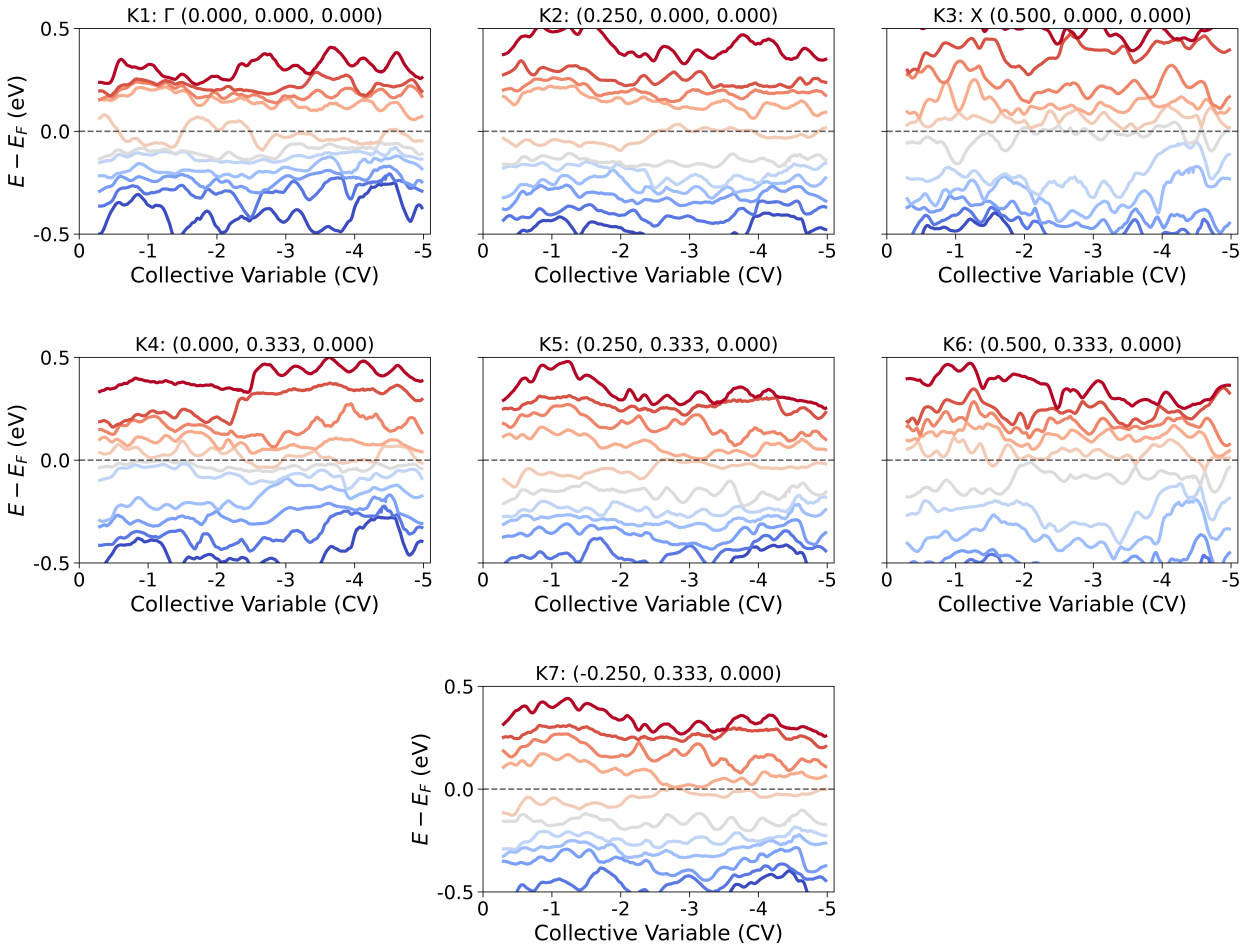

Figure S6: **Electronic Structure Analysis:** Evolution of the band energies for all high-symmetry k-points as a function of the collective variable (CV) under CCM during O-O coupling process.

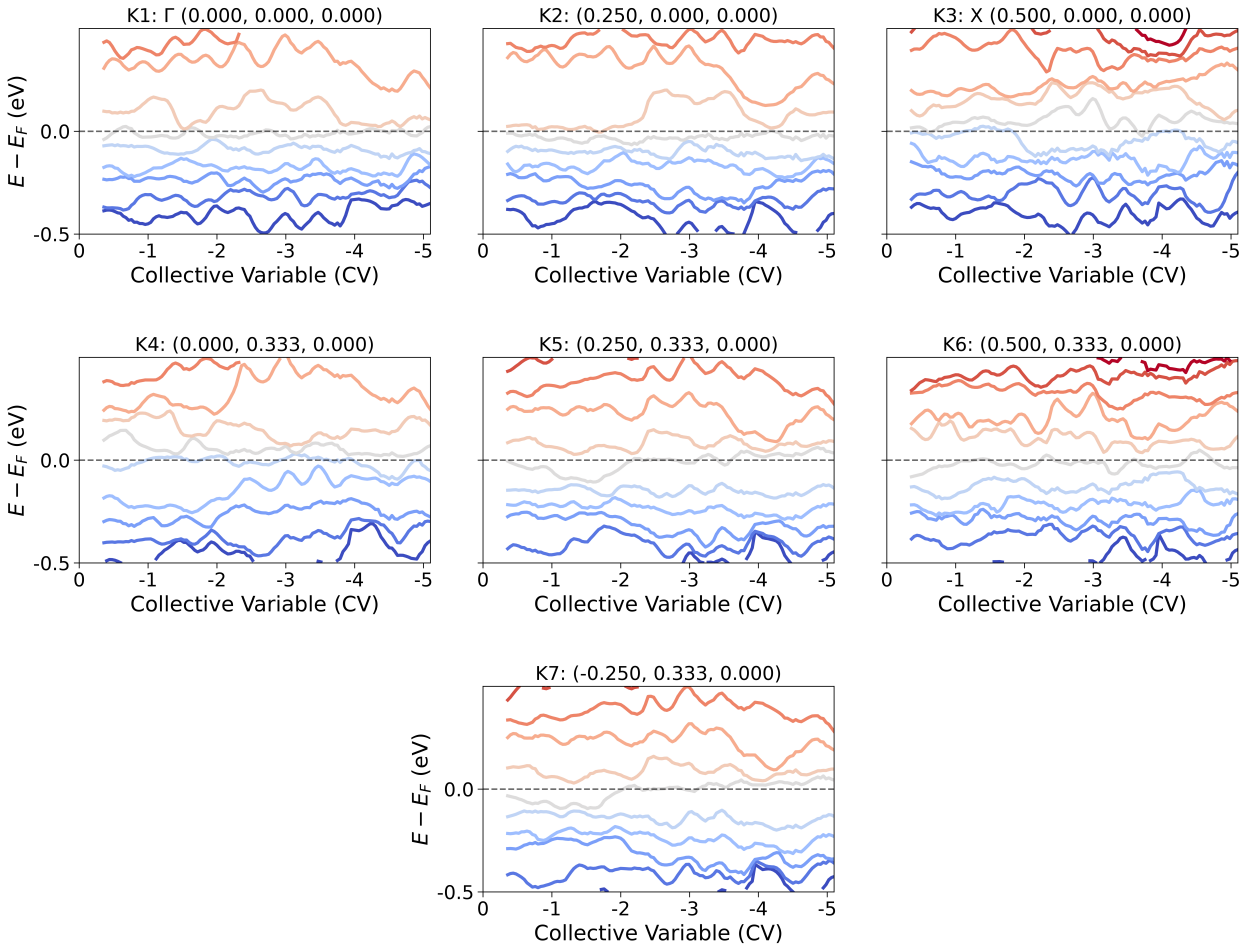

Figure S7: **Electronic Structure Analysis:** Evolution of the band energies for all high-symmetry k-points as a function of the collective variable (CV) under CPM during O-O coupling process.

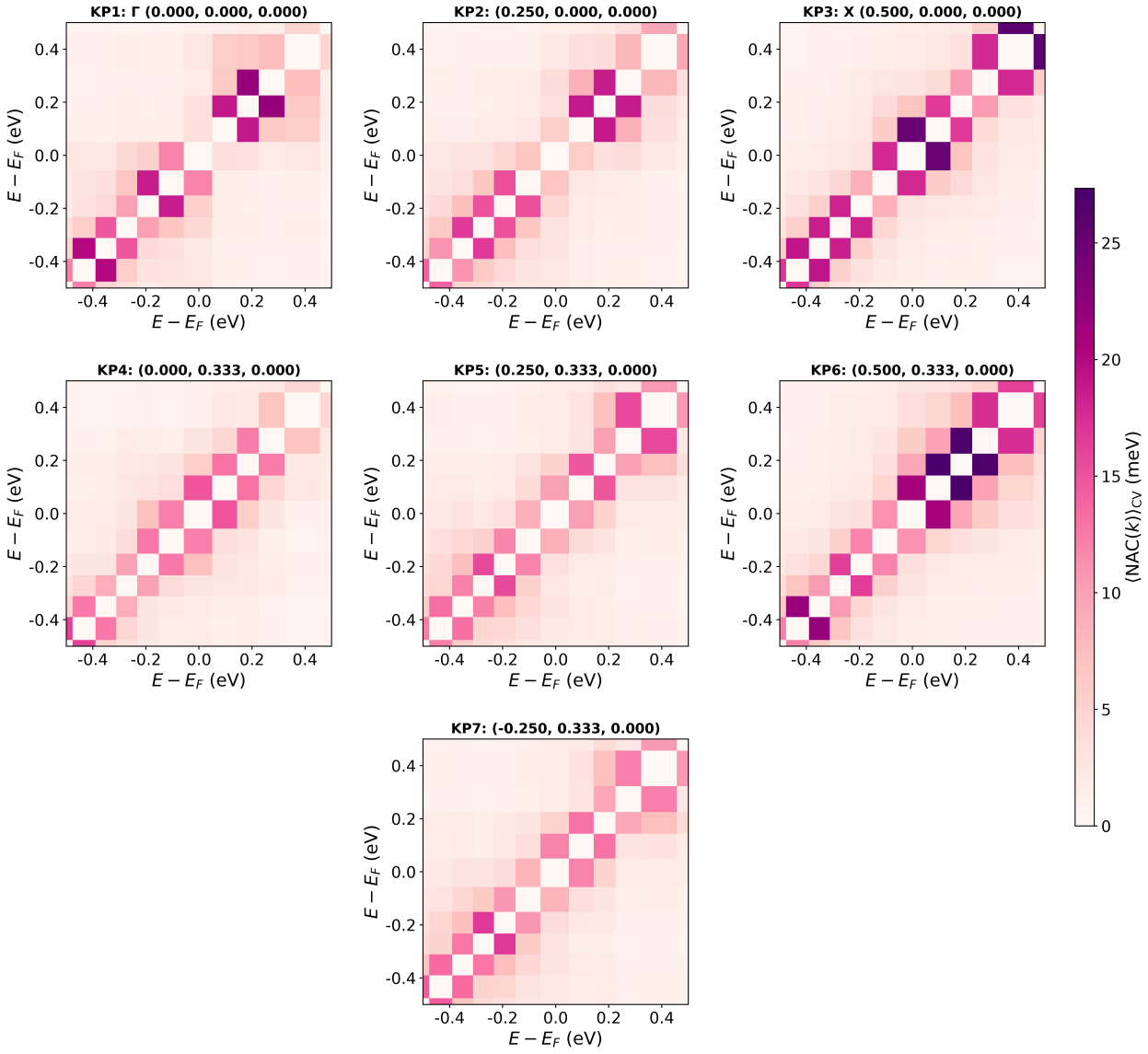

Figure S8: **Non-Adiabatic Coupling Analysis:** The k-point-resolved NAC matrices, averaged over collective-variable configurations sampled along the reaction coordinate under CCM conditions.

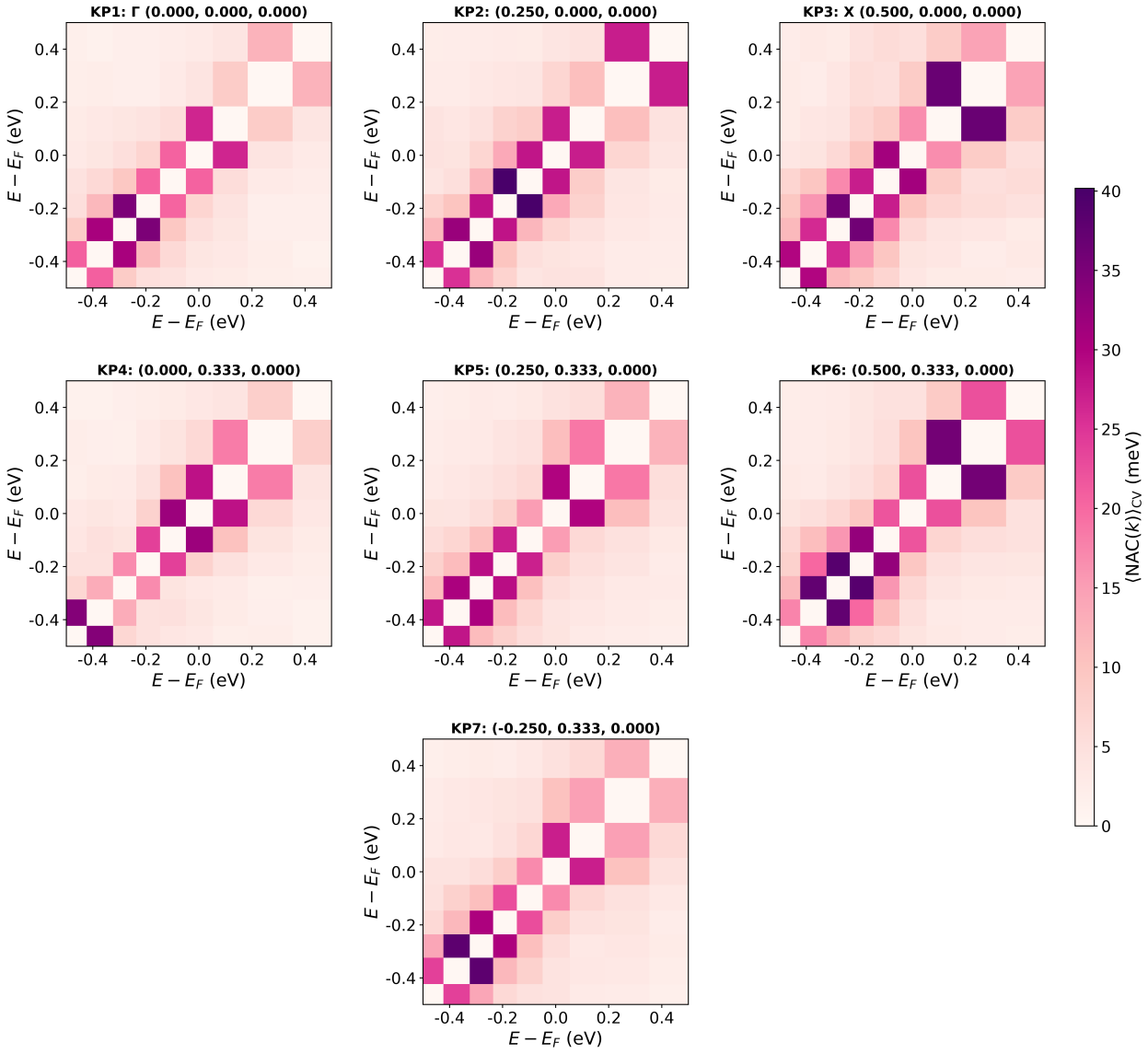

Figure S9: **Non-Adiabatic Coupling Analysis:** The k-point-resolved NAC matrices, averaged over collective-variable configurations sampled along the reaction coordinate under CPM conditions.

References

(1) Kresse, G.; Furthmüller, J. Efficient iterative schemes for ab initio total-energy calculations using a plane-wave basis set. *Physical review B* **1996**, *54*, 11169.

(2) Blöchl, P. E. Projector augmented-wave method. *Physical review B* **1994**, *50*, 17953.

(3) Zhao, X.; Liu, Y. Origin of selective production of hydrogen peroxide by electrochemical oxygen reduction. *Journal of the American Chemical Society* **2021**, *143*, 9423–9428.

(4) Yu, S.; Levell, Z.; Jiang, Z.; Zhao, X.; Liu, Y. What is the rate-limiting step of oxygen reduction reaction on Fe–N–C catalysts? *Journal of the American Chemical Society* **2023**, *145*, 25352–25356.

(5) Mathew, K.; Kolluru, V.; Mula, S.; Steinmann, S. N.; Hennig, R. G. Implicit self-consistent electrolyte model in plane-wave density-functional theory. *The Journal of chemical physics* **2019**, *151*.

(6) Bonnet, N.; Morishita, T.; Sugino, O.; Otani, M. First-principles molecular dynamics at a constant electrode potential. *Physical Review Letters* **2012**, *109*, 266101.

(7) Woo, T. K.; Margl, P. M.; Blöchl, P. E.; Ziegler, T. A combined Car- Parrinello QM/MM implementation for ab initio molecular dynamics simulations of extended systems: application to transition metal catalysis. *The Journal of Physical Chemistry B* **1997**, *101*, 7877–7880.

(8) Carter, E. A.; Ciccotti, G.; Hynes, J. T.; Kapral, R. Constrained reaction coordinate dynamics for the simulation of rare events. *Chemical Physics Letters* **1989**, *156*, 472–477.

(9) Ryckaert, J.-P.; Ciccotti, G.; Berendsen, H. J. Numerical integration of the cartesian equations of motion of a system with constraints: molecular dynamics of n-alkanes. *Journal of computational physics* **1977**, *23*, 327–341.

(10) Jarzynski, C. Nonequilibrium equality for free energy differences. *Physical review letters* **1997**, *78*, 2690.

(11) Chu, W.; Prezhdo, O. V. Concentric approximation for fast and accurate numerical

evaluation of nonadiabatic coupling with projector augmented-wave pseudopotentials. *The Journal of Physical Chemistry Letters* **2021**, *12*, 3082–3089.

(12) Hammes-Schiffer, S.; Tully, J. C. Proton transfer in solution: Molecular dynamics with quantum transitions. *The Journal of chemical physics* **1994**, *101*, 4657–4667.